Spatial Coherence of the Thermal Electromagnetic Field in the vicinity of a Dielectric Slab

Wah Tung Lau[a,b], Jung-Tsung Shen[b], Georgios Veronis[b], and Shanhui Fan[*a,b]
[a]Department of Electrical Engineering, Stanford University, Stanford, CA 94305;
[b]Ginzton Laboratory, Stanford University, Stanford, CA 94305

ABSTRACT

We analyze the spatial coherence of thermal field emitted from a lossy dielectric slab using fluctuation-dissipation theorem.[1] For a given wavelength λ, the coherence property varies drastically with the distance from the slab surface. The coherence length is roughly $\lambda/2$ in the far-field zone, but in the extreme near-field zone, it is many orders of magnitude smaller than λ, due to spatially fluctuating surface charges at the air-dielectric interface. On the other hand, in the intermediate near-field zone, the coherence length can be much longer than $\lambda/2$ if the loss is small, because of the presence of waveguide modes of the slab. Such long-ranged coherence falls off approximately as $1/\sqrt{x}$, in contrast to $1/x$ for a blackbody radiator, where *x* refers to displacement parallel to the slab surface. Furthermore, at a point of fixed distance from the slab surface, the frequency spectrum of the local energy density exhibits distinct fluctuation pattern, which is shown to be closely related to the waveguide dispersion relation.

Keywords: near-field, partial-coherence, spatial-coherence, fluctuation, thermal radiation, dielectric slab, statistical optics, thermo-photovoltaic, waveguide, thermal antenna.

1. INTRODUCTION

An important property of a thermally radiative source is its degree of coherence. In general, the coherence property of such a source is characterized by the cross-spectral density tensor:[2]

$$\overleftrightarrow{W}(\mathbf{r}_1,\mathbf{r}_2,\omega)\delta(\omega-\omega') \equiv \left\langle \vec{E}(\mathbf{r}_1,\omega)\otimes\vec{E}^{*}(\mathbf{r}_2,\omega')\right\rangle, \quad (1)$$

at a given frequency ω. Here $\vec{E}(\mathbf{r},\omega)$ is the spectral Fourier transform of the electric field $\vec{E}(\mathbf{r},t)$. The superscript * indicates the complex conjugate, $\otimes$ is the direct-product of two vectors and the brackets $\langle ... \rangle$ denote a thermal ensemble average.

It was recently recognized that the coherence properties of a thermally radiative body can be drastically different from the blackbody radiator in systems such as microcavities,[3] photonic crystals,[4–9] or in systems exhibiting surface modes [10,11]. Moreover, such changes can be observed both in the near- and the far-field zones. In particular, Carminati *et al.*[11] have shown that in the near field of a polaritonic medium, the range of coherence can be larger than that of the far field and is directly related to the propagating surface polariton mode at the interface between the polaritonic medium and air.[10,11] Such long-ranged coherence property has been shown to be useful, for example, in generating coherent thermal radiation in grating structures.[12] Shchegrov *et al.*[13] demonstrated the spectral changes of the energy density $I(\mathbf{r},\omega)$ of the electric field in the near- and far-field zones of a semi-infinite bulk polaritonic material in the frequency range that supports surface waves. Also, the coherence property of thermal emission in the far field from a dielectric slab has been investigated.[14]

Motivated by these recent developments, here we investigate the spatial coherence of the thermal field in the vicinity of a dielectric slab, with particular emphasis at the near-field zone. In general, one might expect that the waveguide modes in the dielectric slab play an analogous role as the surface waves in the polaritonic media, and thus long-ranged coherence should also be observed in this class of structures. One might further speculate significant differences in the

* Email: shanhui@stanford.edu

Photonic Crystal Materials and Devices VII, edited by Ali Adibi, Shawn-Yu Lin, Axel Scherer,
Proc. of SPIE Vol. 6901, 690109, (2008) · 0277-786X/08/$18 · doi: 10.1117/12.761909

spatial variation ($\mathbf{r}_1 - \mathbf{r}_2$) of the cross-spectral density tensor $\vec{\vec{W}}(\mathbf{r}_1, \mathbf{r}_2, \omega)$ at near- and far-field zones, analogous to the spectral changes in the energy density $I(\mathbf{r}, \omega) = W(\mathbf{r}, \mathbf{r}', \omega)\delta^3(\mathbf{r} - \mathbf{r}')$ for semi-infinite media as in Ref. [13]. Our detailed calculations confirm these expectations. Specifically, three different zones of coherence behavior can be identified:

1. Extreme near-field zone ($z_0 \ll d$), where the spatial coherence length of $\vec{\vec{W}}(\mathbf{r}_1, \mathbf{r}_2, \omega)$ is much less than the wavelength λ. Here d is the $1/e$ amplitude decay length in air of the evanescent tail associated with the guided modes of the slab at frequency ω, $\mathbf{r}_1$ and $\mathbf{r}_2$ are chosen at the same height z_0 from the dielectric slab, and $\lambda = 2\pi c/\omega$ is the wavelength in vacuum.

2. Intermediate near-field zone, where the field shows long-ranged coherence behavior with coherence length larger than $\lambda/2$ when the loss is small. In this low-loss case, the envelope of the trace of the cross-spectral density tensor decays approximately as $1/\sqrt{x}$ for large x, where x refers to displacement parallel to the slab surface.

3. Far-field zone ($z_0 \gg d$): in which the coherence length is $\sim \lambda/2$. The envelope of the cross-spectral density tensor decays approximately as $1/x$.

2. FORMALISM

To begin with, we recapitulate the general notions as in Refs. [11, 13], and then develop the formalism for the specific planar slab geometry of interest. We consider the geometry as shown schematically in Fig. 1. The homogeneous lossy dielectric slab has a finite thickness *a* in the *z* direction $(-a < z < 0)$, and extends infinitely in the *x* and *y* directions. The slab is kept at a uniform temperature *T* in air.

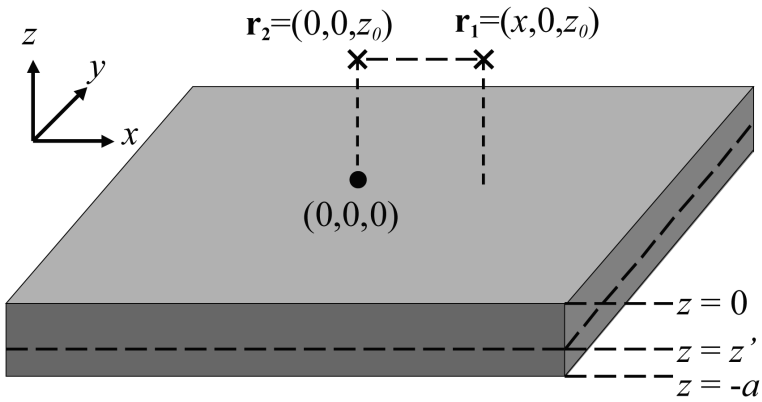

Fig. 1. Schematics of the geometry. The gray region represents the dielectric slab with air above and below. $\mathbf{r}_1$ and $\mathbf{r}_2$ are the two observing points above the slab. A plane $z = z'$ with $-a < z' < 0$ is highlighted by the dashed line.

From the fluctuation-dissipation theorem,[15,16] the presence of loss leads to a fluctuating current density $\vec{j}(\mathbf{r}, t)$ at any point $\mathbf{r} = (x, y, z)$ inside the slab. Such fluctuations are a time-stationary random process. The spectral representation $\vec{j}(\mathbf{r}, \omega)$ is related to its temporal representation by:[17]

$$\vec{j}(\mathbf{r}, t) = \int_{-\infty}^{\infty} [d\omega/(2\pi)]\vec{j}(\mathbf{r}, \omega)e^{-i\omega t}, \tag{2}$$

and $\vec{j}(\mathbf{r}, \omega)$ satisfies the fluctuation-dissipation theorem:[11]

$$\left\langle \vec{j}(\mathbf{r}, \omega) \otimes \vec{j}^{\,*}(\mathbf{r}', \omega') \right\rangle = 4\pi\omega\varepsilon_0\varepsilon''(\omega)\Theta(\omega, T)\delta^3(\mathbf{r} - \mathbf{r}')\delta(\omega - \omega')I$$

where $\vec{\vec{I}}$ is the 3×3 identity matrix, $\Theta(\omega,T)=\hbar\omega/(e^{\hbar\omega/k_BT}-1)$ is the mean energy above the zero-point energy of a quantum harmonic oscillator in thermal equilibrium at temperature *T*, and $\varepsilon''(\omega)$ is the imaginary part of the dielectric constant $\varepsilon(\omega)$. The field radiated into the two half-spaces $z>0$ and $z<-a$ is itself a fluctuating quantity described by a time-stationary random process $\vec{E}(\mathbf{r},t)$. The basic quantity of interest is the second-order coherence of vector fields in the space-time domain:[18]

$$\vec{\vec{\Gamma}}(\mathbf{r}_1,\mathbf{r}_2,\tau)\equiv\left\langle\vec{E}(\mathbf{r}_1,t)\otimes\vec{E}^*(\mathbf{r}_2,t+\tau)\right\rangle, \tag{4}$$

According to the Wiener-Khintchine theorem,[17,19] we can define the cross-spectral density tensor as

$$\vec{\vec{W}}(\mathbf{r}_1,\mathbf{r}_2,\omega)=\int_{-\infty}^{\infty}\vec{\vec{\Gamma}}(\mathbf{r}_1,\mathbf{r}_2,\tau)e^{i\omega\tau}d\tau, \tag{5}$$

It follows that

$$\vec{\vec{W}}(\mathbf{r}_1,\mathbf{r}_2,\omega)\delta(\omega-\omega')=\left\langle\vec{E}(\mathbf{r}_1,\omega)\otimes\vec{E}^*(\mathbf{r}_2,\omega')\right\rangle,$$

as in Eq. (1). Due to mirror symmetry of our system, we only focus on the radiated electric field in the region $z>0$ hereafter. It is related to $\vec{j}(\mathbf{r}',\omega)$ by

$$\vec{E}(\mathbf{r},\omega)=i\mu_0\omega\int_V d^3\mathbf{r}'\vec{\vec{G}}(\mathbf{r},\mathbf{r}',\omega)\vec{j}(\mathbf{r}',\omega), \tag{6}$$

where the integration is performed over the volume *V* of the slab. $\vec{\vec{G}}(\mathbf{r},\mathbf{r}',\omega)$ is the Green dyadic of the considered geometry. Using Eq. (3) and Eq. (6), we obtain

$$\vec{\vec{W}}(\mathbf{r}_1,\mathbf{r}_2,\omega)=4\pi\omega^3{\mu_0}^2\varepsilon_0\varepsilon''(\omega)\Theta(\omega,T)\int_V d^3\mathbf{r}'\vec{\vec{G}}(\mathbf{r}_1,\mathbf{r}',\omega)\vec{\vec{G}}^{\dagger}(\mathbf{r}_2,\mathbf{r}',\omega). \tag{7}$$

Thus to compute $\vec{\vec{W}}(\mathbf{r}_1,\mathbf{r}_2,\omega)$, we need to obtain the expression for $\vec{\vec{G}}(\mathbf{r},\mathbf{r}',\omega)$, which is described below.

By exploiting the translational symmetry of the structure in the *x* and *y* direction, we can decompose $\vec{\vec{G}}(\mathbf{r},\mathbf{r}',\omega)$ into spectral components of spatial wavevector $\boldsymbol{\beta}$ along the two-dimensional *x*-*y* plane. For each component of $\boldsymbol{\beta}$, two independent polarizations can be defined, namely, *s* polarization ($\hat{\mathbf{s}}=\boldsymbol{\beta}\times\hat{\mathbf{z}}$) and *p* polarziation ($\hat{\mathbf{p}}_j=[\beta\hat{\mathbf{z}}+(\gamma_j/\beta)\boldsymbol{\beta}]/\sqrt{(\beta^2+{\gamma_j}^2)}$). Here $\beta=|\boldsymbol{\beta}|$, $\gamma_j=\sqrt{(n_j\omega/c)^2-|\boldsymbol{\beta}|^2}$, where the subscript $j=I$ denotes air and $j=II$ denotes the dielectric material. Hence,

$$G(\mathbf{r},\mathbf{r}',\omega)=\int_{-\infty}^{\infty}\frac{d^2\boldsymbol{\beta}}{4\pi^2}\frac{-i}{2\gamma_{II}}\left[T_s(\beta,z',\omega)\hat{\mathbf{s}}\otimes\hat{\mathbf{s}}+T_p(\beta,z',\omega)\hat{\mathbf{p}}_{\mathbf{I}}\otimes\hat{\mathbf{p}}_{\mathbf{II}}\right]\mathrm{e}^{i\gamma_I z_0-i\gamma_{II}z'}, \tag{8}$$

for $z_0>0$ in the air and $-a<z'<0$ in the slab. $T_\zeta(\beta,z',\omega)$ ($\zeta=s,p$) is the transmission coefficient of the *s*- or *p*-polarized field to free space (denoted by subscript I), from the source plane at $z=z'$ inside the slab (denoted by subscript II), and is given by:[20]

$$T_\zeta(\beta,z',\omega)=\frac{t_\zeta(\beta,\omega)\left[\mathrm{e}^{-i\gamma_{II}z'}+r_\zeta(\beta,\omega)\mathrm{e}^{i\gamma_{II}(2a+z')}\right]}{1-[r_\zeta(\beta,\omega)]^2\,\mathrm{e}^{i2\gamma_{II}a}}. \tag{9}$$

Here $t_\zeta(\beta,\omega)$ and $r_\zeta(\beta,\omega)$ are, respectively the Fresnel transmission and reflection coefficients at a single dielectric-air interface. Specifically, $t_s(\beta,\omega)=2\gamma_{II}/(\gamma_{II}+\gamma_I)$ and $r_s(\beta,\omega)=(\gamma_{II}-\gamma_I)/(\gamma_{II}+\gamma_I)$ for *s* polarization; and $t_p(\beta,\omega)=2n_In_{II}\gamma_{II}/({n_I}^2\gamma_{II}+{n_{II}}^2\gamma_I)$ and $r_p(\beta,\omega)=({n_I}^2\gamma_{II}-{n_{II}}^2\gamma_I)/({n_I}^2\gamma_{II}+{n_{II}}^2\gamma_I)$ for *p* polarization. From Eq. (7) and Eq. (8), $\vec{\vec{W}}(\mathbf{r}_1,\mathbf{r}_2,\omega)$ can be computed.

If we set $\mathbf{r}_1=(x,0,z_0)$ and $\mathbf{r}_2=(0,0,z_0)$. The system would be cylindrically symmetric. It is convenient to define the polar coordinate $\boldsymbol{\beta}=(\beta,\phi)$ and re-express $\vec{\vec{W}}(\mathbf{r}_1,\mathbf{r}_2,\omega)$ as

$$\overleftrightarrow{W}(x,z_0,\omega)=4\pi\omega^3\mu_0{}^2\varepsilon_0\varepsilon''(\omega)\Theta(\omega,T)\int_0^\infty\frac{\beta d\beta}{2\pi}\int_0^{2\pi}\frac{d\phi}{2\pi}\frac{e^{i(\gamma_I-\gamma_I^*)z_0}\,e^{i\beta x\cos\phi}}{4|\gamma_{II}|^2}\int_{-a}^0 dz'$$
$$\left[|T_s(\beta,z',\omega)|^2\begin{pmatrix}\sin^2\phi & -\sin\phi\cos\phi & 0\\ -\sin\phi\cos\phi & \cos^2\phi & 0\\ 0 & 0 & 0\end{pmatrix}\right.$$
$$\left.+|T_p(\beta,z',\omega)|^2\left(\frac{c}{\omega}\right)^4\left(\frac{\beta^2+|\gamma_{II}|^2}{|n_{II}|^2}\right)\begin{pmatrix}|\gamma_I|^2\cos^2\phi & |\gamma_I|^2\cos\phi\sin\phi & -\gamma_I\beta\cos\phi\\ |\gamma_I|^2\cos\phi\sin\phi & |\gamma_I|^2\sin^2\phi & -\gamma_I\beta\sin\phi\\ -\gamma_I^*\beta\cos\phi & -\gamma_I^*\beta\sin\phi & \beta^2\end{pmatrix}\right]. \tag{10}$$

With our choice of coordinate axis, all off-diagonal elements of $\overleftrightarrow{W}(x,z_0,\omega)$ in Eq. (10) are zero after the integration over ϕ. Hence $\overleftrightarrow{W}(x,z_0,\omega)$ is diagonal and the tensorial components of $\overleftrightarrow{W}(x,z_0,\omega)$ are evaluated to be:

$$W_{XX}(x,z_0,\omega)=4\pi\omega^3\mu_0{}^2\varepsilon_0\varepsilon''(\omega)\Theta(\omega,T)\int_0^\infty\frac{\beta d\beta}{2\pi}\frac{e^{i(\gamma_I-\gamma_I^*)z_0}}{4|\gamma_{II}|^2}\int_{-a}^0 dz'$$
$$\left[|T_s(\beta,z',\omega)|^2\frac{J_1(\beta x)}{\beta x}+|T_p(\beta,z',\omega)|^2\left(\frac{c}{\omega}\right)^4\left(\frac{\beta^2+|\gamma_{II}|^2}{|n_{II}|^2}\right)|\gamma_I|^2\left(J_0(\beta x)-\frac{J_1(\beta x)}{\beta x}\right)\right], \tag{11}$$

$$W_{YY}(x,z_0,\omega)=4\pi\omega^3\mu_0{}^2\varepsilon_0\varepsilon''(\omega)\Theta(\omega,T)\int_0^\infty\frac{\beta d\beta}{2\pi}\frac{e^{i(\gamma_I-\gamma_I^*)z_0}}{4|\gamma_{II}|^2}\int_{-a}^0 dz'$$
$$\left[|T_s(\beta,z',\omega)|^2\left(J_0(\beta x)-\frac{J_1(\beta x)}{\beta x}\right)+|T_p(\beta,z',\omega)|^2\left(\frac{c}{\omega}\right)^4\left(\frac{\beta^2+|\gamma_{II}|^2}{|n_{II}|^2}\right)|\gamma_I|^2\frac{J_1(\beta x)}{\beta x}\right], \tag{12}$$

and

$$W_{ZZ}(x,z_0,\omega)=4\pi\omega^3\mu_0{}^2\varepsilon_0\varepsilon''(\omega)\Theta(\omega,T)\int_0^\infty\frac{\beta d\beta}{2\pi}\frac{e^{i(\gamma_I-\gamma_I^*)z_0}}{4|\gamma_{II}|^2}\int_{-a}^0 dz'|T_p(\beta,z',\omega)|^2\left(\frac{c}{\omega}\right)^4\left(\frac{\beta^2+|\gamma_{II}|^2}{|n_{II}|^2}\right)\beta^2 J_0(\beta x). \tag{13}$$

Here J_0 and J_1 are respectively the zeroth and first order Bessel functions of the first kind.

The cross-spectral density tensor can also be expressed by the angular spectrum expansion:[17,21]

$$\overleftrightarrow{W}(x,z_0,\omega)\equiv\int_{-\infty}^\infty\frac{d^2\boldsymbol{\beta}}{4\pi^2}\tilde{\tilde{W}}(\boldsymbol{\beta},z_0,\omega)e^{i\beta x\cos\phi}$$
$$=\int_0^\infty\frac{d\beta}{2\pi}\beta\int_0^{2\pi}\frac{d\phi}{2\pi}e^{i\beta x\cos\phi}\left[\tilde{\tilde{W}}(\beta,\phi,z_0,\omega)\right]. \tag{14}$$

$\tilde{\tilde{W}}$ is the two-dimensional Fourier transform of $\overleftrightarrow{W}$. As we will see later, this expansion of $\overleftrightarrow{W}$ will give considerable physical insights to the underlying physical mechanisms that determine the coherence behavior.

From Eqs. (13) and (14), $\tilde{W}_{ZZ}(\beta,z_0,\omega)$ can be derived as:

$$\tilde{W}_{ZZ}(\beta,z_0,\omega)=4\pi\omega^3\mu_0{}^2\varepsilon_0\varepsilon''(\omega)\Theta(\omega,T)\frac{e^{i(\gamma_I-\gamma_I^*)z_0}}{4|\gamma_{II}|^2}\int_{-a}^0 dz'\left[|T_p(\beta,z',\omega)|^2\left(\frac{c}{\omega}\right)^4\left(\frac{\beta^2+|\gamma_{II}|^2}{|n_{II}|^2}\right)\beta^2\right], \tag{15}$$

which is independent of ϕ. On the other hand, $\tilde{W}_{XX}$ and $\tilde{W}_{YY}$ vary with ϕ in the following manner:

$$\tilde{W}_{XX}(\beta,\phi,z_0,\omega)\propto\sin^2\phi\,|T_s(\beta,z_0,\omega)|^2+\cos^2\phi\,|T_p(\beta,z_0,\omega)|^2\left(\frac{c}{\omega}\right)^4\frac{\beta^2+|\gamma_{II}|^2}{|n_{II}|^2}|\gamma_I|^2, \tag{16}$$

$$\tilde{W}_{YY}(\beta,\phi,z_0,\omega)\propto\cos^2\phi\,|T_s(\beta,z_0,\omega)|^2+\sin^2\phi\,|T_p(\beta,z_0,\omega)|^2\left(\frac{c}{\omega}\right)^4\frac{\beta^2+|\gamma_{II}|^2}{|n_{II}|^2}|\gamma_I|^2. \tag{17}$$

The sum of $\tilde{W}_{XX}$ and $\tilde{W}_{YY}$, however is ϕ independent:

$$\widetilde{W}_{XX}(\beta,\phi,z_0,\omega)+\widetilde{W}_{YY}(\beta,\phi,z_0,\omega)$$
$$=4\pi\omega^3{\mu_0}^2\varepsilon_0\varepsilon''(\omega)\Theta(\omega,T)\frac{e^{i(\gamma_I-\gamma_I^*)z_0}}{4|\gamma_{II}|^2}\int_{-a}^{0}dz'\left[|T_s(\beta,z',\omega)|^2+|T_p(\beta,z',\omega)|^2\left(\frac{c}{\omega}\right)^4\left(\frac{\beta^2+|\gamma_{II}|^2}{|n_{II}|^2}\right)|\gamma_I|^2\right]. \quad (18)$$

The ϕ-independent components of $\beta\widetilde{\vec{W}}$ will be referred to as "β-spectra" hereafter. The pre-factor of β is to account for the linear increase of the two-dimensional density of states with β.

Finally by taking the trace of $\vec{W}$, i.e. $Tr(\vec{W})=W_{XX}+W_{YY}+W_{ZZ}$, we define the coherence length as follows:

$$\xi(z_0,\omega)\equiv\frac{2\int_0^\infty dx\,|Tr[\vec{W}(x,z_0,\omega)]|^2}{|Tr[\vec{W}(x=0,z_0,\omega)]|^2}, \quad (19)$$

3. RESULTS AND INTERPRETATIONS

3.1 Spatial Coherence at various separations from the slab

We now use the formalism developed in Sec. 2 to investigate the coherence properties for the slab geometry. We are interested in the case where the absorption in the slab is small such that the guided modes attenuate slowly. As we will show in the following, these guided modes play a significant role in the coherence properties of the thermal fields. The dielectric constant of the slab is chosen as $12+0.001i$, which approximates that of heavily doped silicon.[22] The slab is assumed to be in air with dielectric constant of 1.

In Fig. 2 we show the dispersion relation of a lossless slab for both polarizations. The horizontal line indicates the frequency $\omega=0.075(2\pi c/a)$, in which all the calculations in this Sec. 3.1 are taken. At this frequency, the slab is single moded for both polarizations. The 1/e decay lengths ($d_\zeta=1/i\gamma_\zeta=1/\sqrt{\beta_\zeta^2-(\omega/c)^2}$, where $\zeta=s,p$) of the guided modes are $6.81a$ for the *s*-polarized mode, and $49.25a$ for the *p*-polarized mode respectively. The decay lengths set the length scale in classifying different zones of z_0 of distinct coherence patterns, as depicted in the Introduction.

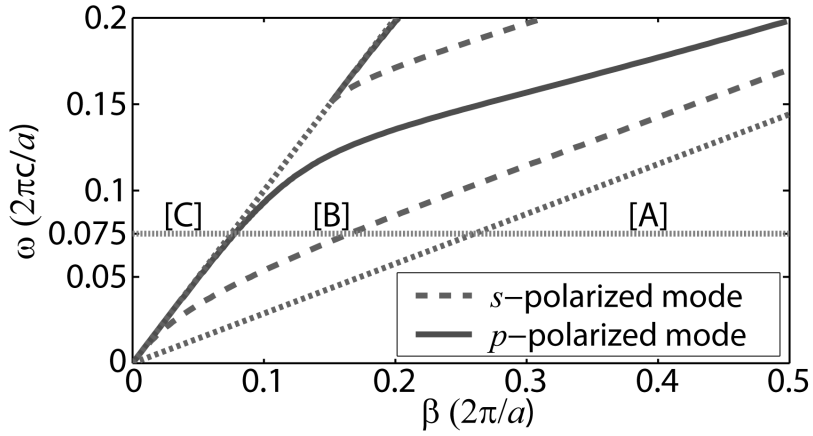

Fig. 2. Dispersion relation of the slab with $n=3.4641$ in air. Here $\beta=|\boldsymbol{\beta}|$. The air ($\omega/c=\beta$) and material ($\omega/c=n\beta$) lightlines are shown, which divide the phase space into Region [A]: $\beta>n\omega/c$, [B]: $\omega/c<\beta<n\omega/c$, and [C]: $\beta<\omega/c$. The operating frequency $\omega=0.075(2\pi c/a)$ is also highlighted.

At a fixed frequency, thermal fields at z_0 consist of waves that are either propagating or evanescent in the direction normal to the slab surface, depending on the spatial wavenumber β. This is seen with reference to Eq. (10), in which $\vec{W}(x,z_0,\omega)$ can be written with integration range separated into $\beta\in[n\omega/c,\infty)$, $\beta\in[\omega/c,n\omega/c]$ and $\beta\in[0,\omega/c]$:

$$\overleftrightarrow{W}(x,z_0,\omega)=\left[\left(\int_{n\omega/c}^{\infty}+\int_{\omega/c}^{n\omega/c}\right)\frac{\beta d\beta}{2\pi}e^{i(\gamma_1-\gamma_1^*)z_0}e^{i\beta x\cos\phi}(...)\right]+\int_0^{\omega/c}\frac{\beta d\beta}{2\pi}e^{i\beta x\cos\phi}(...)$$
$$=\left(\overleftrightarrow{W}^{[A]}+\overleftrightarrow{W}^{[B]}\right)+\overleftrightarrow{W}^{[C]}. \quad (20)$$

The first two terms contain the factor $\exp[i(\gamma_1-\gamma_1^*)z_0]$, which determine the range of z_0 that they dominate. The first term $\overleftrightarrow{W}^{[A]}$, with the range of integration $\beta\in[n\omega/c,\infty)$, describes contributions from waves that are evanescent both inside and outside the slab. In this range of β, the integrand in Eq. (20) appears as a broadband spectrum of β. This gives rise to a narrow peak in $\overleftrightarrow{W}(x,z_0,\omega)$ around $x=0$. This term is significant only when z_0 is very close to zero, i.e. at the "extreme near-field zone". The second term $\overleftrightarrow{W}^{[B]}$ consists of waves with $\beta\in[\omega/c,n\omega/c]$ that are evanescent only outside the slab. Waveguide modes can exist for certain values of β which manifest as poles in the transmission coefficients $|T_{\zeta=s,p}(\beta,z',\omega)|^2$. These poles result in the oscillatory behavior of $\overleftrightarrow{W}(x,z_0,\omega)$ as a function of *x*. $\overleftrightarrow{W}^{[B]}$ is significant when z_0 is comparable to the evanescent decay lengths of the waveguide modes, i.e. at the "intermediate near-field zone". The third term $\overleftrightarrow{W}^{[C]}$ is independent of z_0 as γ_1 is real for $\beta\in[0,\omega/c]$. This term represents the contribution from propagating waves, and dominates in the far field when evanescent waves become negligible.

To elaborate the above physical picture, in Fig. 3-Fig. 6, we show the result of all components of the normalized cross-spectral density tensor $W_{nn}(x,z_0,\omega)/W_{nn}(x=0,z_0,\omega)\big|_{n=X,Y,Z}$ as a function of *x* at some chosen values of z_0, which are respectively at the extreme near-field zone ($z_0=0.001a\ll d$), the intermediate near-field zone ($z_0=0.02a,200a$), and the far-field zone ($z_0=200a\gg d$). The corresponding normalized β-spectra i.e. $\beta[\widetilde{W}_{XX}(\beta,\phi,z_0,\omega)+\widetilde{W}_{YY}(\beta,\phi,z_0,\omega)]/[W_{XX}(x=0,z_0,\omega)+W_{YY}(x=0,z_0,\omega)]$ and $\beta\widetilde{W}_{ZZ}(\beta,z_0,\omega)/W_{ZZ}(x=0,z_0,\omega)$, are also plotted as a function of β. The normalization is such that the integrated area underneath each β-spectral curve, i.e. $\int_0^{\infty}[d\beta/(2\pi)]f(\beta)$, is 1. The operating frequency is fixed at $\omega=0.075(2\pi c/a)$ in all cases.

Fig. 3(a) shows $\overleftrightarrow{W}(x,z_0,\omega)$ as a function of *x*, at $z_0=0.001a$ It is clearly seen that, in this extreme near-field zone, the degree of coherence decreases rapidly with *x* for all W_{XX}, W_{YY} and W_{ZZ}. The coherence length, as defined in Eq. (19) is $\xi=1.13\times10^{-4}\lambda\sim z_0$. This is much smaller than the thickness of the slab, and the skin depth $\lambda/[2\pi\,\mathrm{Im}(n_{II})]$ of the material, which is equal to$1.47\times10^4 a$ for our operating wavelength. The extremely short coherence length here reflects the domination of $\overleftrightarrow{W}^{[A]}$ in Eq. (20). This is reaffirmed in Fig. 3(b), where we plot $\beta\overleftrightarrow{\widetilde{W}}(\beta,z_0,\omega)$ as a function of β. The integral of $\beta\overleftrightarrow{\widetilde{W}}(\beta,z_0,\omega)$ with respect to β is clearly dominated by region [A].

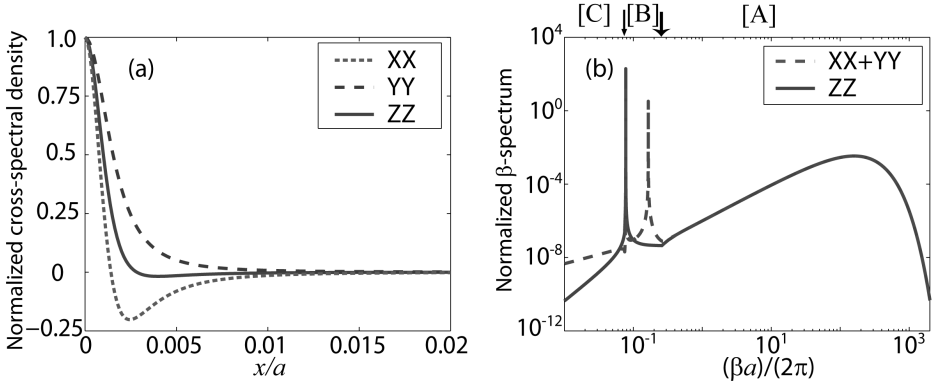

Fig. 3. (a) Components of the normalized cross-spectral density tensor $W_{nn}(x,z_0,\omega)/W_{nn}(x=0,z_0,\omega)\big|_{n=X,Y,Z}$ of the dielectric slab in Fig. 1, as defined in Eqs. (11) - (13) at $z_0=0.001a$ from the slab surface with $\omega=0.075(2\pi c/a)$. (b) Corresponding normalized β-spectra for the in-plane (*XX*+*YY*) and *ZZ* field components, i.e. $\beta[\widetilde{W}_{XX}(\beta,\phi,z_0,\omega)+\widetilde{W}_{YY}(\beta,\phi,z_0,\omega)]/[W_{XX}(x=0,z_0,\omega)+W_{YY}(x=0,z_0,\omega)]$ and $\beta\widetilde{W}_{ZZ}(\beta,z_0,\omega)/W_{ZZ}(x=0,z_0,\omega)$, as defined in Eq. (18) and Eq. (15). The β-space is divided in the same manner as in Fig. 2 with region [A], $\beta>n\omega/c$; Region [B], $\omega/c<\beta<n\omega/c$ and Region [C], $\beta<\omega/c$. The operating frequency is $\omega=0.075(2\pi c/a)$.

Physically, the short range of coherence in the extreme near field can be understood as follows: For *p*-polarized field, the electric field has a *z*-component that is perpendicular to the dielectric-air interfaces. The discontinuity of dielectric constant results in the presence of surface charges at the interface, which are thermally induced and are spatially fluctuating as described by the fluctuating-dissipation theorem. Since the electric field diverges in the vicinity of a point charge, the coherence length becomes very small for the electric field. For *s*-polarized field, the electric field is parallel to the interface and there is no corresponding charge. Hence the coherence length does not approach zero in the extreme near-field zone for purely *s*-polarized field. W_{XX}, W_{YY}, and W_{ZZ}, however, all have contributions from *p*-polarized field as seen in Eqs. (11)-(13), and hence all have very small coherence lengths in this regime.

Fig. 4(a) shows $\overleftrightarrow{W}(x,z_0,\omega)$ at $z_0=0.02a$. In this case, both $\overleftrightarrow{W}^{[A]}$ and $\overleftrightarrow{W}^{[B]}$ contribute significantly. As shown in Fig. 4(b), the areas under the curves of $\beta\widetilde{W}_{mm}(\beta,z_0,\omega)$ in the range $\beta>n\omega/c$ and $\omega/c<\beta<n\omega/c$ are of the same order. As a result, $\overleftrightarrow{W}(x,z_0,\omega)$ shows both features: a narrow peak for small *x* due to $\overleftrightarrow{W}^{[A]}$ and an oscillating behavior for larger *x* attributed to $\overleftrightarrow{W}^{[B]}$. A kink shows up where the narrow peak connects to the oscillatory part. The coherence pattern is therefore characterized by two length scales: one characterizes the width of the narrow peak, and another one characterizes the decaying oscillatory behavior.

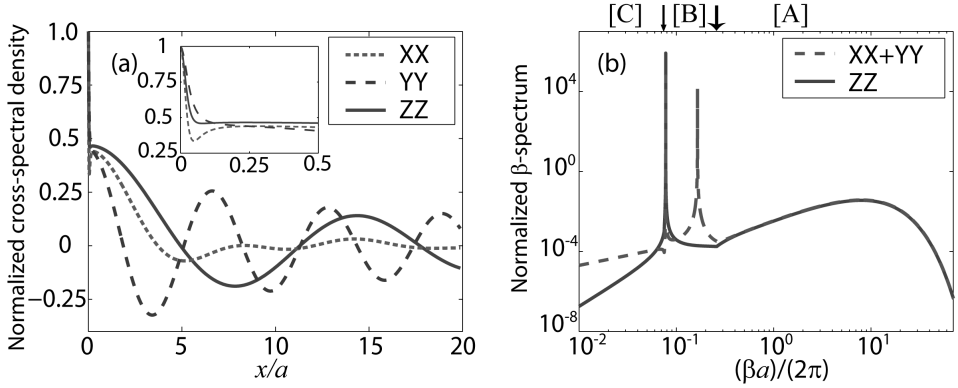

Fig. 4. Same as Fig. 3, except $z_0=0.02a$. The inset in (a) highlights the region $0<x<0.5a$.

Fig. 5(a) shows $\overleftrightarrow{W}(x,z_0,\omega)$ as a function of *x* at $z_0=1a$. This is consistent with Fig. 5(b), which shows that $\overleftrightarrow{W}^{[B]}$, i.e., the area under the curves $\beta\overleftrightarrow{\widetilde{W}}(\beta,z_0,\omega)$ in the range $\beta\in[\omega/c,\mathrm{Re}(n_{II})\omega/c]$, dominates the integral in Eq. (20). The coherence length, $\xi=1.34\lambda$, as calculated from Eq. (19), is longer than $\lambda/2$ of the blackbody.[23] Such enhancement of coherence is due to the slab waveguide modes, as indicated by the dominance of $\overleftrightarrow{W}^{[B]}$. Also seen from Fig. 5(a) is that coherence enhancement occurs in all field components, though with a varying degree. This is distinct from the polaritonic-induced coherence enhancement which occurs only on the *x*-*z* plane.[11]

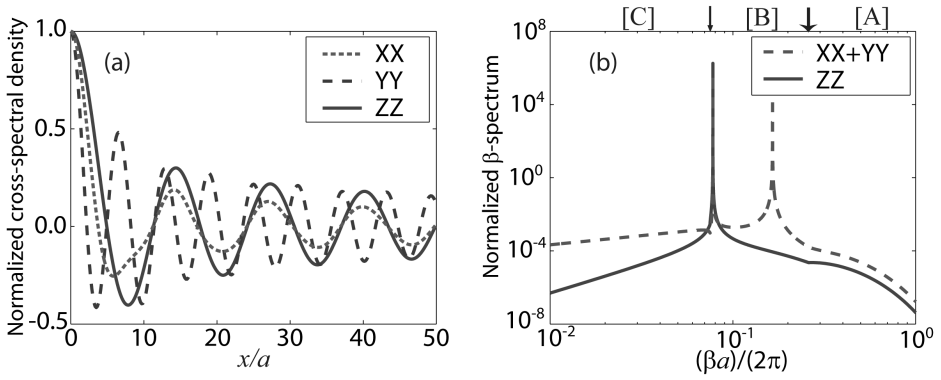

Fig. 5. Same as Fig. 3, except $z_0 = 1a$.

In this regime, nevertheless, all components of the cross-spectral density tensor still decay as a function of *x* because of the following two factors:

(1). In the range $\omega/c < \beta < n\omega/c$, guided modes determine the location of the poles of $|T_s(\beta, z'\omega)|^2$ and $|T_p(\beta, z', \omega)|^2$. These resonance peaks result in the long-ranged oscillatory behavior in the cross-spectral density tensor. When loss is present in the slab, however, these peaks gain finite width and the range of coherence is thus limited.

(2). The second factor for the decay is in fact purely geometrical due to the three-dimensional nature of the problem, and is therefore independent of the loss. In the case where loss in the waveguide is very small, at the lowest order, $\int_{-a}^{0} dz' |T_s(\beta, z', \omega)|^2 \sim a_s \delta(\beta - \beta_s)$, and $\int_{-a}^{0} dz' |T_p(\beta, z', \omega)|^2 \sim a_p \delta(\beta - \beta_p)$ with $0 < a_p, a_s < 1$. a_s and a_p are proportional to the area of the bounded regions by the curve $\widetilde{W}_{XX} + \widetilde{W}_{YY}$ around the *s*- and *p*- poles. Hence, from Eqs. (11) - (13), the components of the cross-spectral density tensor take the following forms:

$$W_{XX}(x, z_0, \omega)\Big|_{\mathrm{Im}(n_{II})\to 0} = f_{XX}(z_0, \omega)\left[a_s(z_0, \omega)\frac{J_1(\beta_s x)}{\beta_s x} + a_p(z_0, \omega)\left(J_0(\beta_p x) - \frac{J_1(\beta_p x)}{\beta_p x} \right) \right] \tag{21}$$

$$W_{YY}(x, z_0, \omega)\Big|_{\mathrm{Im}(n_{II})\to 0} = f_{YY}(z_0, \omega)\left[a_s(z_0, \omega)\left(J_0(\beta_s x) - \frac{J_1(\beta_s x)}{\beta_s x} \right) + a_p(z_0, \omega)\frac{J_1(\beta_p x)}{\beta_p x} \right], \tag{22}$$

$$W_{ZZ}(x, z_0, \omega)\Big|_{\mathrm{Im}(n_{II})\to 0} = f_{ZZ}(z_0, \omega) J_0(\beta_p x). \tag{23}$$

where $f_{XX}(z_0, \omega) = f_{YY}(z_0, \omega)$. Since both $J_0(\beta x)$ and $J_1(\beta x)/(\beta x)$ decrease as a function of x, the components of the cross-spectral density tensor decrease with *x* even when loss is infinitesimal. Moreover, from Eqs. (21) - (23), $Tr[\overleftrightarrow{W}(x)] = W_{XX}(x) + W_{YY}(x) + W_{ZZ}(x) = f_{XX} a_s J_0(\beta_s x) + (f_{XX} a_p + f_{ZZ}) J_0(\beta_p x)$, the envelop of the trace of the cross-spectral density tensor decays asymptotically as $1/\sqrt{x}$ when the loss is small.

Fig. 6(a) and (b) show $\overleftrightarrow{W}(x, z_0, \omega)$ at $z_0 = 200a\ (= 15\lambda)$. At this far-field zone, all contribution from evanescent waves (i.e. $\beta > \omega/c$) becomes negligible. Only the radiative components from Region [C] (i.e. $\beta < \omega/c$) survive, as seen from Fig. 6(b). The coherence length as calculated from Eq. (19) is $\xi = 0.503\lambda$, which is close to the blackbody value,[23] and is smaller than that in the intermediate near-field zone. The envelop of the trace of the cross-spectral density tensor also decays approximately as $1/x$, which is similar to the behavior of a blackbody,[23] but differs from the intermediate near-field zone by an exponent factor of 1/2.

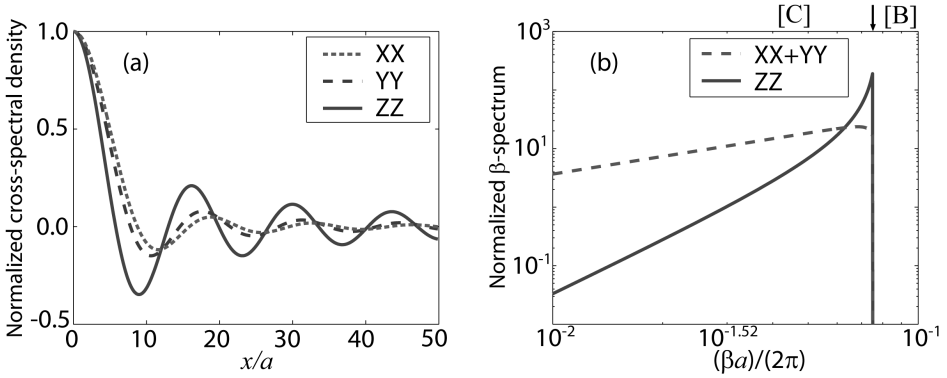

Fig. 6. Same as Fig. 3, except $z_0 = 200a$, and in (b) Region [A] is not shown.

In Fig. 7, we plot the coherence length as a function of z_0 at $\omega = 0.075(2\pi c/a)$, which summarizes the coherence properties of the system. For comparison purposes, the case of a semi-infinite block with the same dielectric constant is also plotted. At the far-field and the extreme near-field zones, the coherence lengths for the two cases almost coincide. The contribution of the waveguide modes is only prominent in the intermediate near-field zone. For $\varepsilon'' = 10^{-3}$, the maximum coherence length is 1.4λ at $z_0 = 6.3a$.

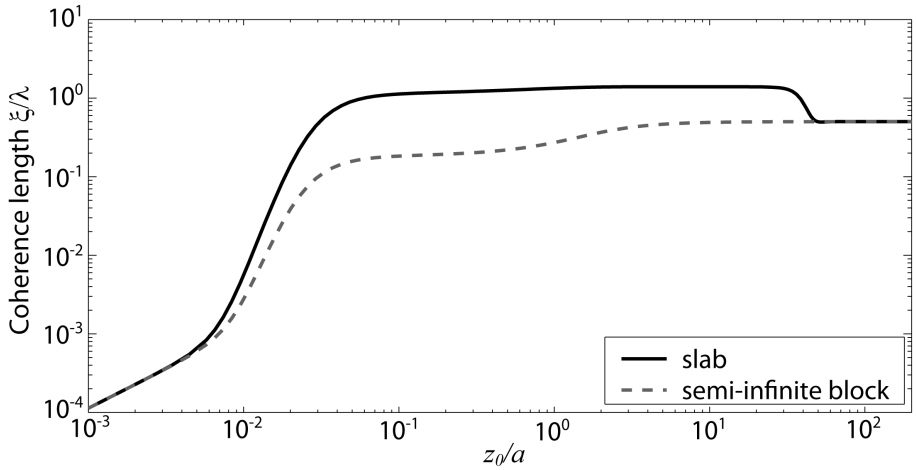

Fig. 7. Coherence length $\xi(z_0)$ as a function of distance z_0 from the air-dielectric interface. Coherence length is calculated according to Eq. (19) with the operating frequency $\omega = 0.075(2\pi c/a)$. The solid line is the case of a slab with thickness a. The dashed line shows the case of the corresponding semi-infinite block, with all material constants the same as in the slab.

3.2 Local energy spectral density at constant separation from the slab

The trace of the cross-spectral density tensor at $x = 0$ is proportional to the local energy spectral density $I(z_0, \omega)$:

$$I(z_0, \omega) \equiv [\varepsilon_0/(2\pi^2)]Tr\left[\overleftrightarrow{W}(x = 0, z_0, \omega)\right]. \tag{24}$$

$I(z_0, \omega)$ is defined such that the energy density at z_0 is $\int_0^\infty d\omega I(z_0, \omega)$. The contribution of each field component to the total local energy spectral density can be seen by expressing Eq. (24) as $I(z_0, \omega) = [\varepsilon_0/(2\pi^2)]\sum_{n=X,Y,Z} W_{nn}(x = 0, z_0, \omega)$ with $W_{XX} = W_{YY}$ at $x = 0$. The quantity $I(z_0, \omega)$ is of interest, for

example, in thermally-induced forces between nano-devices, as well as in near-field spectroscopy.[24, 25] Below we focus on the behavior of $I(z_0,\omega)$ as a function of ω at a fixed distance $z_0 = 1a$ from the slab. The variation of frequency also allows one to span the extreme near-field, the intermediate near-field, and the far-field zones, as previously described.

We define the temperature-independent normalized local energy spectral density $I^{[norm]}(z_0,\omega)$ as:

$$I^{[norm]}(z_0,\omega) = \frac{I(z_0,\omega)}{[\omega^2\Theta(\omega,T)/(2\pi^2c^3)]}, \tag{25}$$

where the normalization factor $\omega^2\Theta(\omega,T)/(2\pi^2c^3)$ is equal to the energy spectral density from a semi-infinite blackbody block with dielectric constant $\varepsilon = \lim_{\varepsilon'\to 1,\varepsilon''\to 0}\varepsilon' + i\varepsilon''$. The 1/2 factor is due to the fact that the radiation only propagates outward from the blackbody. $I^{[norm]}(z_0,\omega)$ is dimensionless and is less than or equal to one at far field. At near field, however, it can exceed 1 due to the contributions from evanescent waves.[24]

In Fig. 8 we plot the normalized $\varepsilon_0 W_{ZZ}(x=0, z_0=1a,\omega)/(2\pi^2)$ and $\varepsilon_0 W_{YY}(x=0, z_0=1a,\omega)/(2\pi^2)$ as a function of ω. In the intermediate near-field zone $0.01(2\pi c/a) < \omega/ < 10(2\pi c/a)$, oscillations arise as a function of frequency. The oscillation pattern can be understood by considering the corresponding dispersion relation of the waveguide modes shown in Fig. 9(a) and (b) for the frequency range of $0.2(2\pi c/a) < \omega < 0.7(2\pi c/a)$, where oscillation pattern is discernible. For the E_y field, which is primarily dominated by contributions from the *s*-polarized wave (and in fact is completely dominated by the *s*-polarized wave at the cut-off), the peaks in energy spectral density coincide with the cutoff frequencies of the *s*-polarized waveguide modes, since at the cutoff of each mode the decay length of the guided mode in air is infinitely large. As the operating frequency moves away from the cutoff, the guided mode shifts away from the light line and the vertical decay length decreases. Thus the local energy spectral density drops accordingly until the cutoff of the next-order guided mode appears.

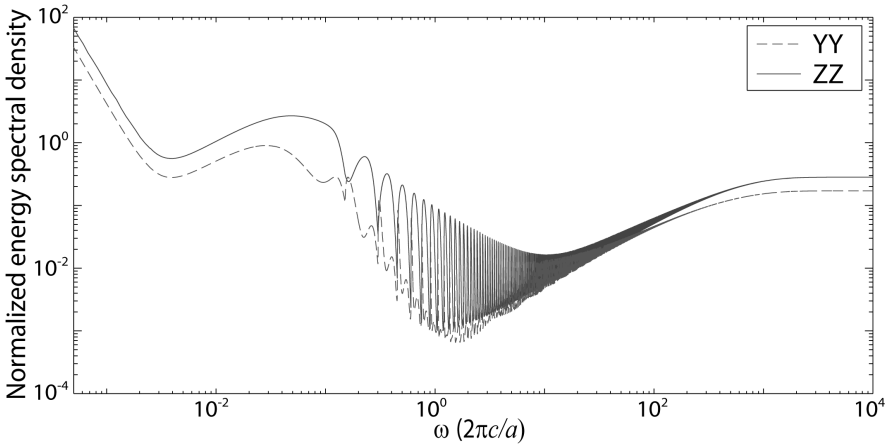

Fig. 8. The plot of *YY* and *ZZ* contributions to the normalized local energy spectral density $I^{[norm]}(z_0,\omega)$ at $z_0 = a$, as a function of ω. The dashed line (*YY*) is $\varepsilon_0 W_{YY}(x=0, z_0=a,\omega)/(2\pi^2)$ and the solid line (*ZZ*) is $\varepsilon_0 W_{ZZ}(x=0, z_0=a,\omega)/(2\pi^2)$ and both are normalized by $\left[\omega^2\Theta(\omega,T)/(2\pi^2c^3)\right]$.

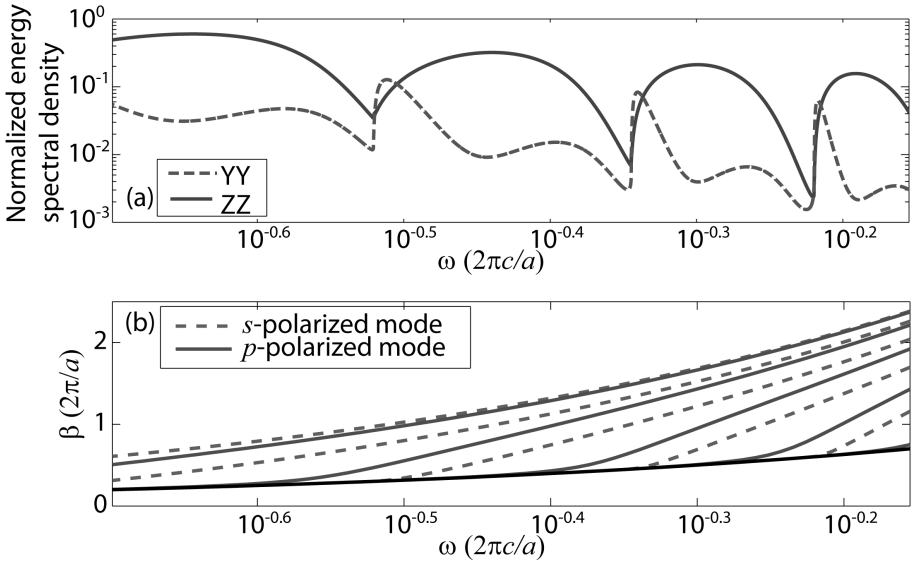

Fig. 9. (a) The *YY* and *ZZ* contributions to the normalized local energy spectral density $I^{[norm]}(z_0,\omega)$ at the range $0.2(2\pi c/a)<\omega<0.7(2\pi c/a)$ which shows oscillatory patterns. (b) The dispersion relation of the corresponding lossless slab of the same thickness with refractive index $n=3.4641$, plotted at the same frequency range of $0.2(2\pi c)/a<\omega/<0.7(2\pi c)/a$, to illustrate the correspondence of the fluctuation pattern in (a) with the *s* and *p* waveguide modes. The lightline $\omega/c=\beta$ is also shown.

We also notice a significant difference in the oscillatory patterns between the E_z and E_y contributions to the total energy spectral density. Note that E_z is totally attributed to the *p*-polarized field, while E_y is related to both *s*- and *p*- polarized fields. Although cutoff frequencies of *s*- and the *p*- polarized modes are the same for each order of waveguide mode, in the immediate vicinity above the cutoffs, the dispersion relation for the *p*-polarized guided modes stays very close to the light line. Hence the energy spectral density from E_z continues to increase as frequency increases, until the dispersion curve of the *p*-polarized guided modes significantly deviates from the light line. Therefore, while the peaks from E_y are located approximately at the cut-offs, the maxima from E_z are located away from the cutoffs. We also note that there are secondary maxima for E_y, with locations approximately coincide with that of the E_z-field. Such maxima arise from contribution of *p*-polarized field. Finally, although not shown here, the total spectral energy density $I(z_0=a,\omega)=\varepsilon_0(2W_{YY}+W_{ZZ})/(2\pi^2)$ also oscillates in the intermediate near-field zone with the same oscillation period in frequency.

In the low frequency limit, when the slab is in the single mode regime, no oscillatory pattern exists and the local energy spectral density increases monotonously at decreasing frequency. This is in fact a signature of the regime of extreme near field, in which energy spectral density increases exponentially with decreased vertical separation from a slab. In the high frequency limit, oscillation disappears as all evanescent components become negligible. In fact, the high frequency limit of the normalized energy spectral density is determined by the emissivity of the slab.

4. CONCLUSION

In summary, we have derived from first principle the coherence property of the radiative thermal field from a uniform dielectric slab with loss. For a given frequency ω, coherence length is extremely short at close proximity from the slab. At a distance of roughly the evanescent length of the waveguide resonances, long-ranged coherence is possible due to slab waveguide modes. At the far-field zone, the coherence length is reduced to approximately $\lambda/2$, which is close to the blackbody value.[23] Also, in the case of small loss (for example $\varepsilon''=10^{-3}$ as in this article), the envelop of the trace of

the cross-spectral density tensor decays approximately as $1/\sqrt{x}$ at the intermediate near field, in contrast to $\sim 1/x$ in the far field, where x refers to displacement parallel to the slab surface.

The existence of long-ranged coherence from a dielectric slab is a significant result, since until now, this effect is known to exist only with special type of materials that allow the formation of surface polaritons.[11] In this article, we show that long-ranged coherence can be achieved for any dielectric slab. Such long-ranged coherence can be exploited to control the spatial and polarization dependence of the coherence in the far field by introducing grating structures on the surface of the dielectric slab. Furthermore, the strong enhancement of the local energy spectral density in the extreme near field may be useful in thermal photovoltaic applications.[5, 26]

REFERENCE

1. W. T. Lau, J. T. Shen, and G. Veronis, S. Fan, Phys. Rev. E 76, 016601 (2007).
2. L. Mandel and E. Wolf, *Optical Coherence and Quantum Optics* (Cambridge University Press, Cambridge, England, 1995), p. 369.
3. I. Celanovic, D. Perreault, and J. Kassakian, Phys. Rev. B 72, 075127 (2005).
4. C. M. Cornelius and J. P. Dowling, Phys. Rev. A 59, 4736 (1999).
5. S. Y. Lin, J. Moreno and J. G. Fleming, Appl. Phys. Lett. 83, 380 (2003).
6. C. Luo, A. Narayanaswamy, G. Chen and J. D. Joannopoulos, Phys. Rev. Lett. 93, 213905 (2004).
7. D. L. C. Chan, M. Soljacic and J. D. Joannopoulos, Phys. Rev. E 74, 036615 (2006).
8. D. L. C. Chan, M. Soljacic and J. D. Joannopoulos, Opt. Express 14, 8785 (2006).
9. M. Laroche, R. Carminati, and J.-J. Greffet, Phys. Rev. Lett. 96, 123903 (2006).
10. C. Henkel, K. Joulain, R. Carminati, and J.-J. Greffet, Opt. Commun. 186, 57 (2000).
11. R. Carminati and J. -J. Greffet, Phys. Rev. Lett. 82, 1660 (1999).
12. J. -J. Greffet, R. Carminati, K. Joulain, J.-P. Mulet, S. Mainguy and Y. Chen, Nature 416, 61 (2002).
13. A. V. Shchegrov, K. Joulain, R. Carminati and J.-J. Greffet, Phys. Rev. Lett. 85, 1548 (2000).
14. X. -G. Liang and M.-H. Han, Chin. Phys. Lett. 23, 1219 (2006).
15. H. B. Callen and T. A. Welton, Phys. Rev. 83, 34 (1951).
16. S. M. Rytov, Yu. A. Kravtsov, and V. I. Tatarskii, *Principles of Statistical Radiophysics 3* (Springer-Verlag, Berlin,1989), p. 118.
17. In this paper the convention of Fourier Transform is $f(x) = \int_{-\infty}^{\infty} [dk/(2\pi)] f(k) e^{ikx}$ for spatial domain and $f(t) = \int_{-\infty}^{\infty} [d\omega/(2\pi)] f(\omega) e^{-i\omega t}$ for temporal domain.
18. L. Mandel and E. Wolf, *Optical Coherence and Quantum Optics* (Cambridge University Press, Cambridge, England, 1995), p. 363.
19. L. Mandel and E. Wolf, *Optical Coherence and Quantum Optics* (Cambridge University Press, Cambridge, England, 1995), p. 59.
20. J. E. Sipe, J. Opt. Soc. Am. B 4, 481 (1987).
21. L. Mandel and E. Wolf, *Optical Coherence and Quantum Optics* (Cambridge University Press, Cambridge, England, 1995), p. 110.
22. R. A. Soref and B. R. Bennett, IEEE J. Quantum Electron. QE-23, 123 (1987).
23. W. H. Carter and E. Wolf, J. Opt. Soc. Am. 65, 1067 (1975).
24. K. Joulain, R. Carminati, J.-P. Mulet and J.-J. Greffet, Phys. Rev. B 68, 245405 (2003).
25. Y. D. Wilde *et. al*., Nature 444, 740 (2006).
26. A. Narayanaswamy and G. Chen, Appl. Phys. Lett. 82, 3544 (2003).